

Fig. 4. Coherence and relaxation of protein spin. (A) Rabi oscillation of single spin label measured by using the sequence in Fig. 1B (fixing τ_0 and RF frequency at middle peak, varying τ). The solid curve is a fit using a sine function with exponential damping. (B) The red circles are measured by the double electron-electron resonance sequences on NV sensor and protein spin (fixing τ equal to spin label π pulse and RF frequency to the central peak, varying τ_0). The black dot is the NV center decoherence curve without protein spin flipping. The solid curves show the best simulation of both of the experimental results in (B), corresponding to a relaxation time of 4 μ s for the spin label and 90 kHz coupling between spin label and NV center.

Relaxation of the protein electron spin is an important parameter to characterize the environment, including information on molecular dynamics. Here, we deduced the longitudinal relaxation time of the spin label from Fig. 4B. The red circles denote the interaction signal between the NV center and the spin label; the black dots show the NV center decoherence curve without operation on the spin label. Simulation (solid curves) shows a relaxation time of 4 μ s. These values are compatible with those for spin labels in ensemble measurements, as the relaxation time of this kind of spin label is \sim 110 μ s at liquid nitrogen temperature (21, 24).

The ability to address single-electron spin labels on proteins adds another element to the emerging diamond sensor-based toolbox for ultra-precise structure determination. Together with the recently established nuclear magnetic resonance (NMR) detection, the present method extends the sensing range to dozens of nanometers, whereas diamond sensor-based NMR only senses nuclear spins in very close proximity (a few nanometers) to the NV center (26–29). The interaction between the spin label and the neighboring nuclei could be used to sense more distant nuclei and provide structural and dynamical information otherwise inaccessible by the sensor. In this respect, it is particularly encouraging that we find long spin relaxation times enabling coherent spin driving at the protein. This capability will allow the use of the ancillary electron spin for sophisticated coherent control (30, 31), thereby facilitating future polarization transfer experiments that could gain access to nuclear spins in proteins, including proton or ^{13}C spins. When combined with either scanning magnetometry or nanoscale magnetic resonance imaging based on magnetic field gradients, protein structure analysis under ambient conditions at the level of a single molecule is within reach (32, 33).

REFERENCES AND NOTES

1. L. Redecke et al., *Science* **339**, 227–230 (2013).
2. T. R. M. Barends et al., *Nature* **505**, 244–247 (2014).
3. M. C. Scott et al., *Nature* **483**, 444–447 (2012).
4. C. C. Chen et al., *Nature* **496**, 74–77 (2013).
5. P. P. Borbat, A. J. Costa-Filho, K. A. Earle, J. K. Moscicki, J. H. Freed, *Science* **291**, 266–269 (2001).

6. D. Rugar, R. Budakian, H. J. Mamin, B. W. Chui, *Nature* **430**, 329–332 (2004).
7. M. Xiao, I. Martin, E. Yablonovitch, H. W. Jiang, *Nature* **430**, 435–439 (2004).
8. Y. Manassen, R. J. Hamers, J. E. Demuth, A. J. Castellano Jr., *Phys. Rev. Lett.* **62**, 2531–2534 (1989).
9. G. Balasubramanian et al., *Nature* **455**, 648–651 (2008).
10. J. R. Maze et al., *Nature* **455**, 644–647 (2008).
11. J. M. Taylor et al., *Nat. Phys.* **4**, 810–816 (2008).
12. G. Balasubramanian et al., *Nat. Mater.* **8**, 383–387 (2009).
13. N. Bar-Gill, L. M. Pham, A. Jarmola, D. Budker, R. L. Walsworth, *Nat. Commun.* **4**, 1743 (2013).
14. M. S. Grinolds et al., *Nat. Phys.* **9**, 215–219 (2013).
15. B. Grotz et al., *New J. Phys.* **13**, 055004 (2011).
16. A. O. Sushkov et al., *Nano Lett.* **14**, 6443–6448 (2014).
17. L. S. Michel et al., *Nature* **409**, 355–359 (2001).

18. S. Martin-Lluesma, V. M. Stucke, E. A. Nigg, *Science* **297**, 2267–2270 (2002).
19. M. W. Doherty et al., *Phys. Rep.* **528**, 1–45 (2013).
20. F. Z. Shi et al., *Phys. Rev. B* **87**, 195414 (2013).
21. See supplementary materials on Science Online.
22. V. Gaponenko et al., *Protein Sci.* **9**, 302–309 (2000).
23. J. A. Weil, J. R. Bolton, *Electron Paramagnetic Resonance: Elementary Theory and Practical Applications* (Wiley, New York, ed. 2, 2007), pp. 316–317.
24. K. Jacobsen, S. Oga, W. L. Hubbell, T. Risse, *Biophys. J.* **88**, 4351–4365 (2005).
25. M. A. Hemminga, L. J. Berliner, *ESR Spectroscopy in Membrane Biophysics* (Springer Science and Business Media, New York, 2007), pp. 133–134.
26. T. Staudacher et al., *Science* **339**, 561–563 (2013).
27. H. J. Mamin et al., *Science* **339**, 557–560 (2013).
28. F. Z. Shi et al., *Nat. Phys.* **10**, 21–25 (2014).
29. C. Müller et al., *Nat. Commun.* **5**, 4703 (2014).
30. M. Schaffry, E. M. Gauger, J. J. L. Morton, S. C. Benjamin, *Phys. Rev. Lett.* **107**, 207210 (2011).
31. A. O. Sushkov et al., *Phys. Rev. Lett.* **113**, 197601 (2014).
32. M. S. Grinolds et al., *Nat. Nanotechnol.* **9**, 279–284 (2014).
33. L. Luan et al., <http://arxiv.org/abs/1409.5418> (2014).

ACKNOWLEDGMENTS

We thank F. Jelezko for helpful discussions. Supported by 973 Program grants 2013CB921800 and 2012CB917202, National Natural Science Foundation of China grants 11227901, 91021005, 31470835, 11275183, and 21103199, and the Chinese Academy of Sciences. J.W. was supported by the Max Planck Society and the European Union (via the ERC grants SQUITEC and DIADEMS) and by the Baden-Württemberg Stiftung.

SUPPLEMENTARY MATERIALS

www.sciencemag.org/content/347/6226/1135/suppl/DC1
Materials and Methods
Tables S1 and S2
Figs. S1 to S7
References (34–37)

3 November 2014; accepted 29 January 2015
10.1126/science.aaa2253

BRAIN STRUCTURE

Cell types in the mouse cortex and hippocampus revealed by single-cell RNA-seq

Amit Zeisel,^{1,*} Ana B. Muñoz-Manchado,^{1,*} Simone Codeluppi,¹ Peter Lönnerberg,¹ Gioele La Manno,¹ Anna Juréus,¹ Sueli Marques,¹ Hermany Munguba,¹ Liquan He,² Christer Betsholtz,^{2,3} Charlotte Rolny,⁴ Gonçalo Castelo-Branco,¹ Jens Hjerling-Leffler,^{1,†} Sten Linnarsson^{1,†}

The mammalian cerebral cortex supports cognitive functions such as sensorimotor integration, memory, and social behaviors. Normal brain function relies on a diverse set of differentiated cell types, including neurons, glia, and vasculature. Here, we have used large-scale single-cell RNA sequencing (RNA-seq) to classify cells in the mouse somatosensory cortex and hippocampal CA1 region. We found 47 molecularly distinct subclasses, comprising all known major cell types in the cortex. We identified numerous marker genes, which allowed alignment with known cell types, morphology, and location. We found a layer I interneuron expressing *Pax6* and a distinct postmitotic oligodendrocyte subclass marked by *Itpr2*. Across the diversity of cortical cell types, transcription factors formed a complex, layered regulatory code, suggesting a mechanism for the maintenance of adult cell type identity.

The brain is built from a large number of specialized cell types, enabling highly refined electrophysiological behavior, as well as fulfilling brain nutrient needs and defense against pathogens. Functional specialization

allows fine-tuning of circuit dynamics and decoupling of support functions such as energy supply, waste removal, and immune defense. Cells in the nervous system have historically been classified using location, morphology, target specificity, and

electrophysiological characteristics, often combined with molecular markers (1–5). Systematic in situ hybridization has revealed extensive regional heterogeneity (6). However, none of these properties carry enough information to result, in every case, in a definitive cell type identification (7). Single-cell RNA sequencing (RNA-seq) has been used to classify cells in spleen (8), lung epithelium (9), and embryonic brain (10). However, the adult nervous system has greater complexity and more cell types, presenting a challenge both to sample preparation methods and computational analysis.

Here, we have used quantitative single-cell RNA-seq (11) to perform a molecular census of the primary somatosensory cortex (S1) and the hippocampal CA1 region, based on 3005 single-cell transcriptomes (Fig. 1A and fig. S1, A to C). Individual RNA molecules were counted using unique molecular identifiers (UMIs) (essentially tags that identify individual molecules) (12) (figs. S1, D to J, and S2, A to E) and confirmed by single-molecule RNA fluorescence in situ hybridization (FISH) (fig. S2, G to I).

We used clustering to discover molecularly distinct classes of cells. Standard hierarchical clustering resulted in fragmented clusters (fig. S4), because most genes were not informative in most pairwise comparisons and contributed at

best only noise. Biclustering can overcome this problem by simultaneously clustering genes and cells. We developed BackSPIN (see the supplementary materials), a divisive biclustering method based on sorting points into neighborhoods (SPIN) (13), which revealed nine major classes of cells: S1 and CA1 pyramidal neurons, interneurons, oligodendrocytes, astrocytes, microglia, vascular endothelial cells, mural cells (that is, pericytes and vascular smooth muscle cells), and ependymal cells (Fig. 1, A and B, and fig. S3).

The data set allowed us to identify the most specific markers for each class, many of which are known to play a functional role in these cells (fig. S5). S1 pyramidal cells were marked by *Tbr1*, a transcription factor required for the final differentiation of cortical projection neurons; oligodendrocytes by *Hapln2*, encoding a protein required for proper formation of nodes of Ranvier; mural cells by *Acta2*, a key component of actin thin filaments; and endothelial cells by *Ly6c1* [expressed by monocytes peripherally, and endothelial cells in the brain (14)]. Some were novel, such as *Gm11549* (a long noncoding RNA specific to S1 pyramidal neurons), *Spink8* (a serine protease inhibitor specific to hippocampal pyramidal cells), and *Pnoc* (prepronociceptin, here identified as an interneuron marker).

By repeating biclustering on each of the nine major classes (Fig. 1C and figs. S5 to S8), we identified a total of 47 molecularly distinct subclasses of cells. Every subclass was detected in multiple mice (fig. S1K), arguing that cell identity was preserved across these genetically outbred (CD-1) mice. Neurons contained more RNA than glia and vascular cells and a larger number of detectable genes (Fig. 1C and fig. S1E). Mitochondrial mRNAs were less variable, although mitochondrial tRNAs were highly specifically enriched in endothelial cells (fig. S1E).

We identified seven subclasses of S1 pyramidal cells (Fig. 2A and figs. S6A and S7), which were largely layer-specific. The superficial layers II/III and IV were represented by single populations, whereas layer V showed two distinct subclasses. Layers VI and VIb were represented by single populations, but in addition we found a subclass lacking specific markers but expressing common deep-layer markers such as *Pcp4*. A distinct subclass expressed *Synpr* and *Nr4a2*, which are abundant in the adjacent claustrum, with some cells extending into S1.

We found two types of CA1 glutamatergic cells (fig. S8), plus cells derived from the adjacent CA2 (as defined by *Pcp4*) and subiculum (as defined by *Ly6g6e*). Genes highly expressed in type 2 CA1 pyramidal neurons were associated with mitochondrial function (fig. S8), which has been shown to correlate with the firing rate and length of projections in cortical neurons (15). Orthogonal to the two main classes, we found CA1 layer-specific markers (i.e., *Calb1* and *Nov*), as well as dorsoventrally patterned genes (i.e., *Wfs1* and *Grp*) (16), in both of the two main types of CA1 cells. These may correspond to functional differences between layers (17).

We found 16 subclasses of interneurons (Fig. 2B and fig. S6, C and D), but there are likely more subclasses because we achieved only shallow sampling of *Sst*- and *Pvalb*-expressing cells. In superficial layers of S1, we identified an *Htr3a*- and *Pax6*-expressing interneuron subclass, confirmed by immunohistochemistry (Fig. 2C) [$13.9 \pm 2.4\%$ of serotonin (5HT) receptor 3a-enhanced green fluorescent protein (5HT3aEGFP) cells in layer I, $n = 4$ mice, 636 cells analyzed]. These interneurons specifically expressed *Myh8*, *Fut9*, and *Manea*. In whole-cell current clamp recordings of layer I neurons, subsequently stained for PAX6, these cells exhibited intrinsic electrophysiological and

¹Division of Molecular Neurobiology, Department of Medical Biochemistry and Biophysics, Karolinska Institutet, S-171 77 Stockholm, Sweden. ²Department of Immunology, Genetics and Pathology, Rudbeck Laboratory, Uppsala University, Dag Hammarskjölds väg 20, S-751 85 Uppsala, Sweden. ³Division of Vascular Biology, Department of Medical Biochemistry and Biophysics, Karolinska Institutet, S-171 77 Stockholm, Sweden. ⁴Department of Oncology-Pathology, Karolinska Institutet, S-171 76 Stockholm, Sweden.

*These authors contributed equally to this work. †Corresponding author. E-mail: sten.linnarsson@ki.se (S.L.); jens.hjerling-leffler@ki.se (J.H.-L.)

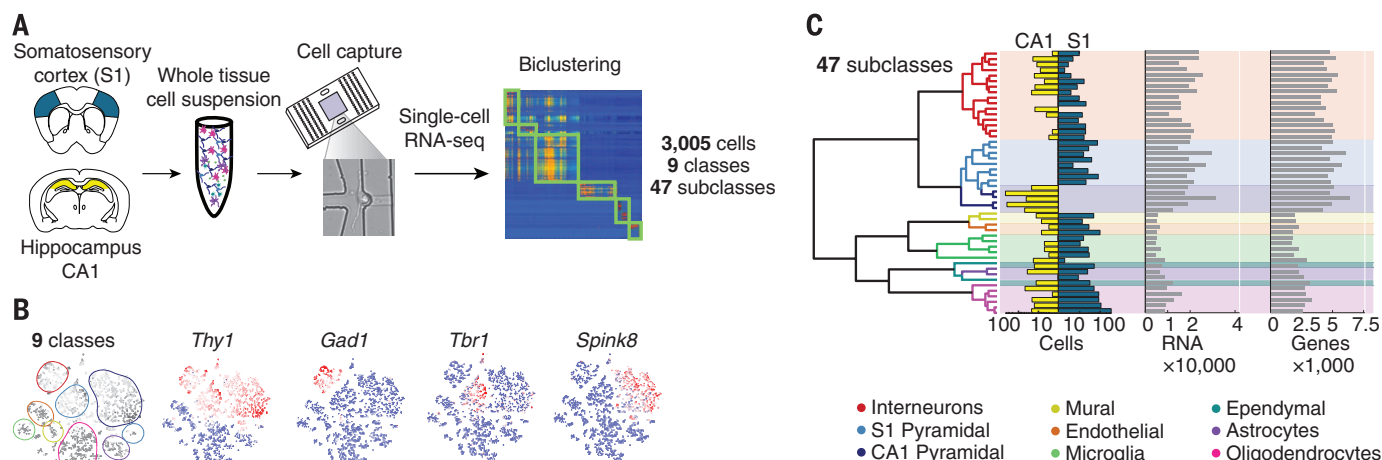


Fig. 1. Molecular census of somatosensory S1 cortex and hippocampus CA1 by unbiased sampling and single-cell RNA-seq. (A) Workflow for obtaining and analyzing single-cell RNA-seq from juvenile mouse cortical cells, from dissection to single-cell RNA-seq and biclustering. (B) Visualization of nine major classes of cells using t-distributed stochastic neighbor embedding (tSNE). Each dot is a single cell, and cells are laid out to show similarities. Colored contours correspond to the nine clusters in (A) and fig. S3. Expression of known markers is shown using the same layout (blue, no expression; white, 1% quantile; red, 99% quantile). (C) Hierarchical clustering analysis on 47 subclasses. Bar plots show number of captured cells in CA1 and S1, number of detected polyA+ RNA molecules per cell, and total number of genes detected per cell.

morphological characteristics of late-spiking neurogliaform cells (6 PAX6⁺ out of 40 recorded cells) (Fig. 2D and fig. S6E). *Pax6* is not expressed in the ventral forebrain during development, further suggesting that neurogliaform cells are developmentally heterogeneous (18).

CA1 and S1 regions both contained interneurons of almost every subclass (Fig. 2B), showing that interneurons residing in functionally distinct cortical structures are transcriptionally closely related. The two exceptions were cells expressing *Vip*, *Penk*, *Calb2*, and *Crh* (which were confined to S1) and cells expressing *Lhx6*, *Reln*, and *Gabrd* [which were confined to CA1 and may be medial ganglionic eminence-derived Ivy cells and neurogliaform cells (18)].

Astrocytes formed two subclasses (Fig. 3A and fig. S9A) distinguished by differential expression of *Gfap* (type 1) and *Mfge8* (type 2). Immunostaining showed that type 1 astrocytes were derived from

layer I, particularly from the glia limitans, a thin layer made up mostly of astrocytes that is arranged against the pia (Fig. 3B). In contrast, type 2 astrocytes were more uniformly distributed in the cortex and were smaller and less ramified.

We identified two types of immune cells: microglia (the tissue-resident macrophages of the brain) and perivascular macrophages. Although closely related, these cell types have distinct developmental origin (19). Both expressed brain macrophage markers *Aif1* and *Cx3cr1*, whereas perivascular macrophages were distinguished by expression of *Mrc1* and *Lyve1*, characteristic of pro-angiogenic perivascular type 2 macrophages (20). Immunohistochemistry for the corresponding proteins confirmed that microglia (AIF1⁺/LYVE1⁺/MRC1⁺) had a classical, ramified morphology and were located throughout the cortex (Fig. 3, D and E). In contrast, perivascular macrophages (AIF⁺/LYVE1⁺/MRC1⁺) were located

only along vessels and showed an ameboid morphology. They were distinct from mural and endothelial cells (fig. S10). Comparison with peritoneal macrophages confirmed their identity (fig. S9A). The correlation between brain and peripheral macrophages (0.67) was similar to that between neurons and glia (0.62), underscoring the functional divergence of this immune cell class.

Six subpopulations of oligodendrocytes were identified (Fig. 3F and fig. S9C), likely representing stages of maturation: immature (Oligo4), premyelinating (Oligo2), myelinating (Oligo5), and terminally differentiated postmyelination (Oligo6) oligodendrocytes. An intermediate population, Oligo3, was almost exclusively observed in somatosensory cortex and may represent a distinct cellular state specific for this tissue. The subclass Oligo1, which did not express the prototypical genes associated with oligodendrocyte precursor cells (OPCs), may represent a postmitotic cellular state, associated with the first steps of oligodendrocyte differentiation. Oligo1 cells expressed a distinct set of genes, including *Itpr2*, *Prom1*, *Gpr17*, *Tef7l2*, *9630013A20Rik*, *Idh1*, *Cnksr3*, and *Rnf122*. Single-molecule RNA FISH confirmed that *Itpr2* and *Cnksr3* were expressed in strict subsets of cells expressing *Plp1*, a pan-oligodendrocyte marker (4.5% and 7.5%, respectively) (Fig. 3G). Together, the Oligo1 to Oligo6 populations may represent sequential steps in the process of maturation from an OPC to a terminally differentiated oligodendrocyte.

Across this diverse set of cell types, we found many transcription factors with highly restricted expression patterns (Fig. 4A and supplementary materials). For example, interneurons expressed key interneuron regulators *Dlx1*, *Dlx2*, *Dlx5*, and *Arx*, and pyramidal layer II/III neurons expressed *Neurog2*, which can directly reprogram human embryonic stem cells to excitatory neurons of layer II/III phenotype with near 100% efficiency (21). *Lyl1* and *Spic* were specific to perivascular macrophages; *Spic* is essential for the maintenance of red pulp macrophages (22), suggesting that it may play a similar role in brain perivascular macrophages.

Expanding this analysis to all genes, we found extensive functional specialization between cellular subclasses. Ependymal cells (multiciliated cells lining the ventricles) expressed the largest set of subclass-restricted genes, including transcription factors *Foxj1*, *Myb*, and *Rfx2*, the master regulators of motile ciliogenesis (23) (24), and *Zmynd10*, which causes ciliopathy when mutated in humans (25). Nearly every structural component of cilia was also represented (Fig. 4B), including the 2+9 microtubule core and radial spokes, the dynein and kinesin motors, the filamentous shell, the basal body that anchors cilia to the cytoplasm, and two adenylate kinases (*Ak7* and *Ak8*) that generate adenosine triphosphate energy supporting cilia motility. Many of these structural genes are directly regulated by *Foxj1*, *Rfx2*, or *Rfx3* (23, 26) (Fig. 4B).

In summary, our findings reveal the diversity of brain cell types and transcriptomes. Across the full set of cell types, transcription factors formed a complex, layered regulatory code, suggesting a

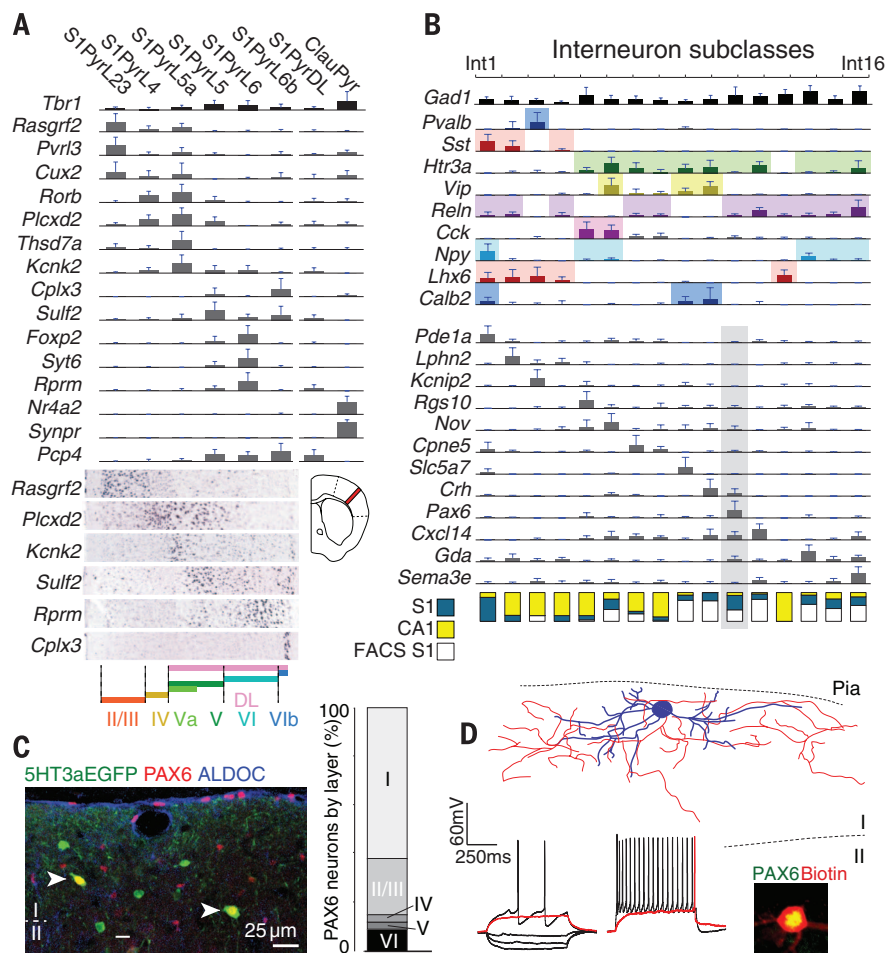


Fig. 2. Neuron subclasses in the somatosensory cortex. (A) Subclasses of pyramidal neurons in the somatosensory cortex (S1) identified by BackSPIN clustering. Bar plots show mean expression of selected known and novel markers (error bars show standard deviations). Layer-specific expression shown by in situ hybridization (Allen Brain Atlas). S1PyrL23, layer II-III; S1PyrL4, layer IV; S1PyrL5a, layer Va; S1PyrL5, layer V; S1PyrL6, layer VI; S1PyrL6b, layer VIB; S1PyrDL, deep layers; ClauPyr, claustrum. (B) Identification of interneuron subclasses. Bar plots show selected known and novel markers. Fraction of S1/CA1 cells is depicted at bottom: blue, S1; yellow, CA1; white, flow-sorted Htr3a⁺ cells from S1. (C) Immunohistochemistry demonstrating the existence and localization of novel PAX6⁺/5HT3aEGFP⁺ interneurons, Int11. Bar plots show the layer distribution of these neurons. (D) Intrinsic electrophysiology and morphology of PAX6⁺ interneurons in S1 layer I, identified by post hoc staining.

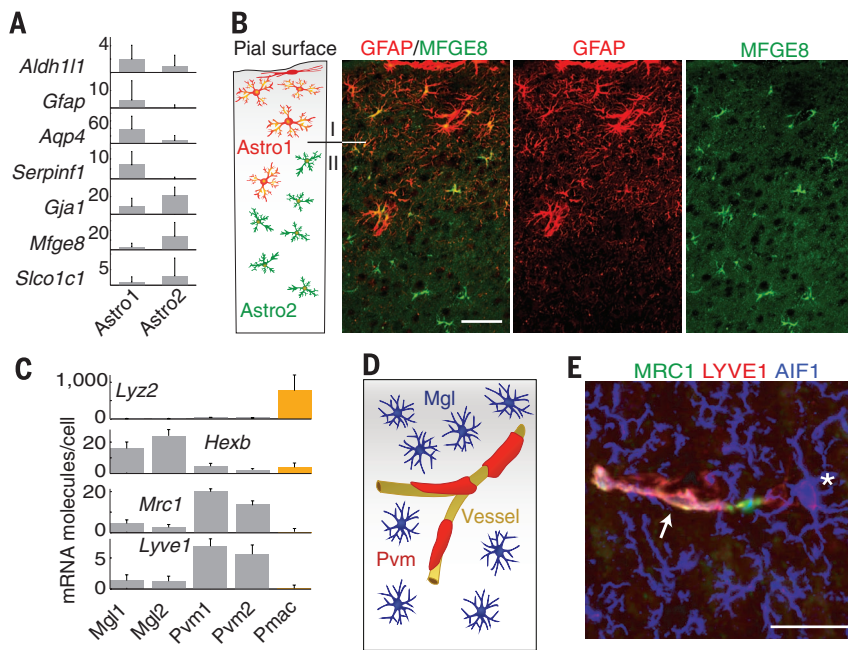


Fig. 3. Characterization of glial subclasses. (A) Two types of astrocytes (Astro1 and Astro2) identified by common and distinct markers. (B) Immunohistochemistry for glial fibrillary acidic protein (red, Astro1) and MFGE8 (green, Astro2). Scale bar, 50 μ m. (C) Genes showing expression restricted to microglia (Mgl), perivascular macrophages (Pvm), and peritoneal macrophages (Pmac). Error bars show standard deviations. (D) Cartoon illustrating the morphology and localization of microglia and perivascular macrophages. (E) Immunostaining for AIF1 (previously known as Iba-1, blue) marking microglia, and for MRC1 (green) and LYVE1 (red) marking perivascular macrophages. Asterisk, a microglia cell. Arrow, a perivascular macrophage aligned to a vessel (not stained). Scale bar, 20 μ m. (F) Heat map showing progressive changes in gene expression along oligodendrocyte differentiation, illustrated below. (G) Single-molecule RNA FISH for *Itpr2* and *Cnksr3* mark a strict subset of oligodendrocytes (as identified by *Plp1*). Scale bar, 11 μ m.

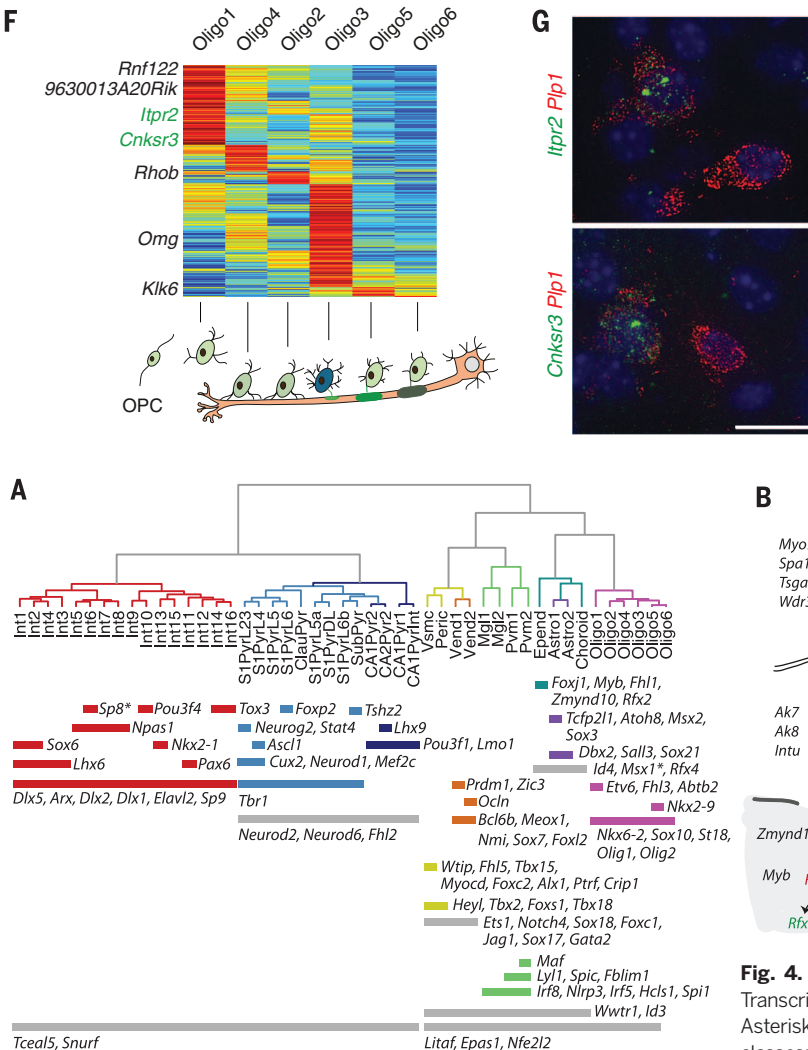


Fig. 4. Expression of regulatory genes across 47 subclasses. (A) Transcription factors showing restricted expression across cell types. Asterisks denote genes with additional expression in distinct subclasses: *Sp8* in *Int11*, *Msx1* in vascular cells and microglia. (B) Genes

specific to ependymal cells. Transcription factors *Foxj1*, *Rfx2*, and *Rfx3* (with asterisk to indicate its wider expression) and their known targets are shown in red, green, and blue, respectively. Arrows indicate known direct interactions between transcription factors. Only genes with known ciliary function are included.

plausible mechanism for the maintenance of adult differentiated cell types. More broadly, these results showcase the power of explorative single-cell RNA-seq and point the way toward future whole-brain and even whole-organism cell type discovery and characterization. Such data will deepen our understanding of the regulatory basis of cellular identity, in development, neurodegenerative disease, and regenerative medicine.

REFERENCES AND NOTES

1. B. J. Molyneaux, P. Ariotta, J. R. Menezes, J. D. Macklis, *Nat. Rev. Neurosci.* **8**, 427–437 (2007).
2. T. Klausberger, P. Somogyi, *Science* **321**, 53–57 (2008).
3. J. DeFelipe et al., *Nat. Rev. Neurosci.* **14**, 202–216 (2013).
4. K. Sugino et al., *Nat. Neurosci.* **9**, 99–107 (2006).
5. G. Fishell, B. Rudy, *Annu. Rev. Neurosci.* **34**, 535–567 (2011).
6. E. S. Lein et al., *Nature* **445**, 168–176 (2007).
7. A. Kepecs, G. Fishell, *Nature* **505**, 318–326 (2014).
8. D. A. Jaitin et al., *Science* **343**, 776–779 (2014).
9. B. Treutlein et al., *Nature* **509**, 371–375 (2014).
10. A. A. Pollen et al., *Nat. Biotechnol.* **32**, 1053–1058 (2014).
11. S. Islam et al., *Nat. Methods* **11**, 163–166 (2014).
12. T. Kivioja et al., *Nat. Methods* **9**, 72–74 (2011).
13. D. Tsafir et al., *Bioinformatics* **21**, 2301–2308 (2005).
14. C. Shi, E. G. Pamer, *Nat. Rev. Immunol.* **11**, 762–774 (2011).
15. O. Kann, C. Huchzermeyer, R. Kovács, S. Wirtz, M. Schuelke, *Brain* **134**, 345–358 (2011).
16. H. W. Dong, L. W. Swanson, L. Chen, M. S. Fanselow, A. W. Toga, *Proc. Natl. Acad. Sci. U.S.A.* **106**, 11794–11799 (2009).
17. K. Mizuseki, K. Diba, E. Pastalkova, G. Buzsáki, *Nat. Neurosci.* **14**, 1174–1181 (2011).
18. L. Tricoire et al., *J. Neurosci.* **30**, 2165–2176 (2010).
19. M. Prinz, J. Priller, *Nat. Rev. Neurosci.* **15**, 300–312 (2014).
20. I. Galea et al., *Glia* **49**, 375–384 (2005).
21. Y. Zhang et al., *Neuron* **78**, 785–798 (2013).
22. M. Kohyama et al., *Nature* **457**, 318–321 (2009).
23. J. A. Thomas et al., *Biol. Cell* **102**, 499–513 (2010).
24. E. R. Brooks, J. B. Wallingford, *Curr. Biol.* **24**, R973–R982 (2014).
25. M. A. Zarivwala et al., *Am. J. Hum. Genet.* **93**, 336–345 (2013).
26. M. I. Chung et al., *eLife* **3**, e01439 (2014).

ACKNOWLEDGMENTS

The raw data have been deposited with the Gene Expression Omnibus (www.ncbi.nlm.nih.gov/geo) under accession code GSE60361. Annotated data are available at <http://linnarssonlab.org/cortex>. We thank P. Ernfors, K. Harris, and R. Sandberg for useful comments on the manuscript; F. Ginhoux for helpful discussions on microglia and macrophages; A. Johnsson for laboratory management and support; ALM/SciLife (H. G. Blom) for technical support; and Fluidigm Inc. (R. C. Jones and M. Lynch) for generous technical and instrument support. S.L. was supported by the European Research Council (261063, BRAINCCELL) and the Swedish Research Council (STARGET); A.Z. was supported by the Human Frontier Science Program; A.B.M.-M. was supported by the Karolinska Institutet (BRECT); C.R. was supported by the Swedish Cancer Society (CAN2013/852); G.C.-B. was supported by the Swedish Research Council, the European Union (FP7/Marie Curie Integration Grant EPIOPC), the Åke Wiberg Foundation, the Karolinska Institutet Research Foundations, Svenska Läkaresällskapet, Clas Groschinskys Minnesfond, and Hjärtfonden; J.H.-L. was supported by the Swedish Research Council, the European Union (FP7/Marie Curie Actions (322304, Adolescent Development)), StratNeuro, and the Jeanssons, Åke Wibergs, and Magnus Bergvalls Foundations; C.B. was supported by the European Research Council (294556, BBBARRIER), a Knut and Alice Wallenberg Scholar Grant, the Swedish Cancer Society, and Swedish Research Council. Supplementary materials contain additional data.

SUPPLEMENTARY MATERIALS

www.sciencemag.org/content/347/6226/1138/suppl/DC1
Materials and Methods
Supplementary Text
Figs. S1 to S11
Tables S1 and S2
References (27–36)

30 October 2014; accepted 30 January 2015
Published online 19 February 2015;
10.1126/science.aaa1934

FRESHWATER ECOLOGY

Experimental nutrient additions accelerate terrestrial carbon loss from stream ecosystems

Amy D. Rosemond,^{1*} Jonathan P. Benstead,² Phillip M. Bumpers,¹ Vladislav Gulis,³ John S. Kominoski,^{1†} David W. P. Manning,¹ Keller Suberkropp,² J. Bruce Wallace¹

Nutrient pollution of freshwater ecosystems results in predictable increases in carbon (C) sequestration by algae. Tests of nutrient enrichment on the fates of terrestrial organic C, which supports riverine food webs and is a source of CO₂, are lacking. Using whole-stream nitrogen (N) and phosphorus (P) additions spanning the equivalent of 27 years, we found that average terrestrial organic C residence time was reduced by ~50% as compared to reference conditions as a result of nutrient pollution. Annual inputs of terrestrial organic C were rapidly depleted via release of detrital food webs from N and P co-limitation. This magnitude of terrestrial C loss can potentially exceed predicted algal C gains with nutrient enrichment across large parts of river networks, diminishing associated ecosystem services.

Nutrient pollution of freshwater ecosystems is pervasive and strongly affects carbon (C) cycling. Excess nutrients stimulate the production of C-rich algal biomass but can also stimulate C loss through increased organic C mineralization that releases CO₂ instead of supporting production of higher trophic levels and other ecosystem functions (1, 2). Production of aquatic life in freshwater ecosystems is based on algae and organic C of terrestrial origin. Currently, consideration of nutrient effects on C cycling in inland waters has focused on enhancement of algal C sinks in lakes and less on fates of terrestrial C that may experience accelerated loss in river networks (3–5).

The processes that lead to nutrient stimulation of algal C production and terrestrial C mineralization are fundamentally different. Algal production increases relatively predictably with the availability of growth-limiting nutrients (1, 6). In contrast, mineralization of particulate organic C (POC) is the more complex result of activity by multiple trophic levels consisting of microbial decomposers and detritivorous animals (hereafter detritivores) (7). Inputs of leaves and wood are the main sources of POC in many rivers, supporting production of animals and uptake of inorganic pollutants (8–10). Nutrients stimulate microbial processing of POC, which results in increased losses of CO₂ to the atmosphere (2, 11). Consumption of microbially colonized POC by detritivores further contributes to its breakdown and conversion to smaller particles, which affect its subsequent transport and processing downstream (7).

To determine how moderate nutrient pollution affects terrestrially derived POC at stream-

reach scales, we tested how long-term (2- to 5-year), continuous, flow-proportional nitrogen (N) and phosphorus (P) additions affected its loss rates and fates in headwater forest streams (12). We measured the response of terrestrial C loss rates in whole 70- to 150-m stream reaches (tables S1 and S2). Carbon loss rates at this spatial scale are a function of biologically driven breakdown and hydrological export and have not been previously assessed in response to human-influenced stressors (13). We conducted two manipulative experiments at large spatial and temporal scales and focused our measurements on forest-derived leaf litter, because it is the most biologically active pool of terrestrial C in forest streams and is renewed annually (7). After a pretreatment year, we enriched one stream with N and P at a set ratio for 5 years in a paired watershed design (N+P experiment; a second stream acted as a control) and used expanded N and P gradients in a second experiment in five other streams for 2 years after a pretreatment year (N×P experiment) (table S1).

Reach-scale terrestrial C loss rates increased with N and P enrichment across all the concentrations we tested (Fig. 1). Discharge, N, P, temperature, and associated random effects (stream and year) explained 83% of the variation in C loss rates across 27 annual measurements (table S3). Standardized regression coefficients indicated that our moderate additions of N and P contributed roughly three-fourths of the effect on litter loss rates as annual cumulative discharge, which varied 87-fold across streams and years (table S3). Nitrogen and P ($r = 0.79$) and discharge and temperature ($r = -0.76$) were correlated, so their effects and relative significance cannot be teased apart fully. However, roughly similar-sized effects of N and P on loss rates are strong evidence of co-limitation (Fig. 2 and table S3). Comparisons of loss rates from corresponding enriched and reference streams indicate that median C loss rates increased 1.65 times with nutrient enrichment (table S4); the range in these values (1.02 to 4.49 times) reflects variation due to N

¹Odum School of Ecology, University of Georgia, Athens, GA 30602, USA. ²Department of Biological Sciences, University of Alabama, Tuscaloosa, AL 35487, USA. ³Department of Biology, Coastal Carolina University, Conway, SC 29528, USA.

*Corresponding author. E-mail: rosemond@uga.edu †Present address: Department of Biological Sciences, Florida International University, Miami, FL 33199, USA.